

# 3D printed self-supporting elastomeric structures for multifunctional microfluidics

Ruitao Su<sup>1</sup>, Jiaxuan Wen<sup>2</sup>, Qun Su<sup>2</sup>, Michael S. Wiederoder<sup>3</sup>, Steven J. Koester<sup>2</sup>, Joshua R. Uzarski<sup>3</sup>, Michael C. McAlpine<sup>1\*</sup>

Microfluidic devices fabricated via soft lithography have demonstrated compelling applications such as lab-on-a-chip diagnostics, DNA microarrays, and cell-based assays. These technologies could be further developed by directly integrating microfluidics with electronic sensors and curvilinear substrates as well as improved automation for higher throughput. Current additive manufacturing methods, such as stereolithography and multi-jet printing, tend to contaminate substrates with uncured resins or supporting materials during printing. Here, we present a printing methodology based on precisely extruding viscoelastic inks into self-supporting microchannels and chambers without requiring sacrificial materials. We demonstrate that, in the submillimeter regime, the yield strength of the as-extruded silicone ink is sufficient to prevent creep within a certain angular range. Printing tool-paths are specifically designed to realize leakage-free connections between channels and chambers, T-shaped intersections, and overlapping channels. The self-supporting microfluidic structures enable the automatable fabrication of multifunctional devices, including multimaterial mixers, microfluidic-integrated sensors, automation components, and 3D microfluidics.

## INTRODUCTION

Microfluidic devices have the potential to enable transformational approaches for conducting microliter-scale chemical and biological research because of the advantages of small sample volumes and well-controlled microenvironments (1). They have demonstrated exciting applications in areas such as lab-on-a-chip diagnostics (2), point-of-care systems (3), organ replication on a chip (4), and bioassays (5). The two most widely used methodologies for the fabrication of microfluidic devices are soft lithography and additive manufacturing. Soft lithography is a microfabrication-based method that can achieve submicron resolution in devices, which are typically fabricated using the elastomer polydimethylsiloxane (PDMS) (6, 7). However, the requirement of microfabrication facilities, stamp distortions, and time-consuming manual steps such as PDMS molding, layer alignment, and bonding imposes constraints on the use of soft lithography to produce ubiquitous and widely deployable microfluidic devices (8). Additive manufacturing, or three-dimensional (3D) printing, techniques have recently emerged as promising complements or alternatives to augment the manufacturability of microfluidic devices (9). Comparative advantages of additive manufacturing techniques include the potential for autonomous and portable manufacturing, rapid prototyping, and the ability to incorporate freeform 3D structures (10). Several 3D printing approaches have been used for the fabrication of microfluidic devices. Stereolithography (SL) is one extensively studied method that uses photocurable resins to create well-defined microchannels with feature sizes below 100 μm and a range of components for fluid manipulation (11). Multi-jet modeling (MJM) fabricates microfluidic devices via inkjet printing ultraviolet (UV)-polymerizable inks and has the capability for printing multiple materials (12). However, because of the potential for contamination from either uncured residual resin in the channel voids or the sacrificial

supporting materials temporarily used to form hollow structures, directly printing microfluidic structures onto substrates that contain predeposited 3D structures or electronic sensing elements is challenging for SL and MJM. The degree of automation of SL and MJM is also compromised because of the postprocessing required to remove the residual precursor and supporting materials from the channels. In addition, microfluidic devices printed by SL and MJM with photocurable resins have low elasticity and cannot be aligned to existing structures.

Extrusion-based 3D printing provides a freeform method to fabricate objects via the conformal deposition of filaments onto target surfaces (13). To date, it has not been extensively investigated for elastomeric microfluidics even though the multifunctionality of this method has been realized via numerous classes of functional materials and devices, such as fully 3D printed optoelectronic device arrays (14), conformal channels for isolation of biomarkers (15), and cell-laden biological constructs (16, 17). The challenge of directly printing hollow structures with viscoelastic inks lies in the insufficient mechanical strength of uncured polymers to counter the creep of as-printed structures (18, 19). This normally requires the use of sacrificial supporting materials (20). One possible solution is to print part of the wall structure and enclose the roofs of the devices with flat glass covers, but this imposes planar and rigid constraints on the form factor of the resulting device (21). To create hollow structures without supporting materials or exterior covers, two factors should be controlled to ensure that the maximum stress within the self-supporting structures is less than the yield strength of the as-extruded ink: (i) At least one dimension of the hollow space should be relatively small, from several millimeters to hundreds of micrometers, to reduce the total gravitational loading, and (ii) the yield strength should be sufficiently high, tens of Pascals or higher (22), to balance the gravitational loading of the overhung part.

Here, we introduce an automatable extrusion-based printing methodology that can directly align and print elastomeric microfluidic structures onto planar and curvilinear substrates with minimal involvement of postprocessing. By selecting inks of proper yield strength and controlling the profiles of printed overhung structures,

Copyright © 2020  
The Authors, some  
rights reserved;  
exclusive licensee  
American Association  
for the Advancement  
of Science. No claim to  
original U.S. Government  
Works. Distributed  
under a Creative  
Commons Attribution  
NonCommercial  
License 4.0 (CC BY-NC).

<sup>1</sup>Department of Mechanical Engineering, University of Minnesota, Minneapolis, MN 55455, USA. <sup>2</sup>Department of Electrical and Computer Engineering, University of Minnesota, Minneapolis, MN 55455, USA. <sup>3</sup>U.S. Army Combat Capabilities Development Command Soldier Center, Natick, MA 01760, USA.

\*Corresponding author. Email: mcalpine@umn.edu

self-supporting walls can be realized and further enclosed to form hollow structures such as channels and chambers. Since the microfluidic spanning distance is in the submillimeter regime, a sufficiently small bending moment results that the as-printed walls can withstand, rendering this method suitable for printing microfluidic structures. Printing toolpaths can then be designed to create leakage-free transitions between channels and chambers, T-shaped intersections, and overlapping channels. This methodology eliminates supporting materials and channel covers that are conventionally required to build hollow structures with viscoelastic materials, enabling multi-material mixers and microfluidic-integrated salinity sensors via direct integration with predeposited features such as herringbone (HB) ridges and sensing microelectrodes. We also printed 3D microfluidic networks integrated with valves on a spherical surface, demonstrating a previously unrealized device form factor that opens opportunities for implementation on freeform surfaces such as the human body for microfluidic-based wearable health sensors. The devices demonstrated in this work serve as a proof of concept for the automatable capabilities of extrusion-based 3D printing to fabricate self-supporting and aligned multifunctional microfluidic structures.

## RESULTS

### Self-supporting microfluidic structures

Our hypothesis was that self-supporting walls can be printed with the extrusion-based 3D printing method via carefully designed filament stacking orientations, e.g., straight or circular, on the cross-sectional planes (Fig. 1A). The walls merged at the top and formed hollow channels and chambers with targeted geometries specified by the printing toolpath in the X-Y plane, such as the triangular/circular channels and hexagonal/conical domes illustrated in the bottom panel of Fig. 1A. For the ink, we selected an acetoxy silicone that is room temperature vulcanizing (RTV) when exposed to moisture in the air. This one-part silicone is ready to use without prior mixing or other preparation and cures in ambient environment without requiring UV irradiation or thermal heating. Because of its high biocompatibility, oxygen permeability, chemical resistance, and elastomeric properties, silicone has been widely used for microfluidic devices that are fabricated by soft lithography (6, 23). In addition, cured RTV silicone structures demonstrate high elongation before breaking and good adhesion to different surfaces (fig. S1). The Young's modulus was found to be, on average,  $189.7 \pm 5.6$  kPa ( $N = 3$ ).

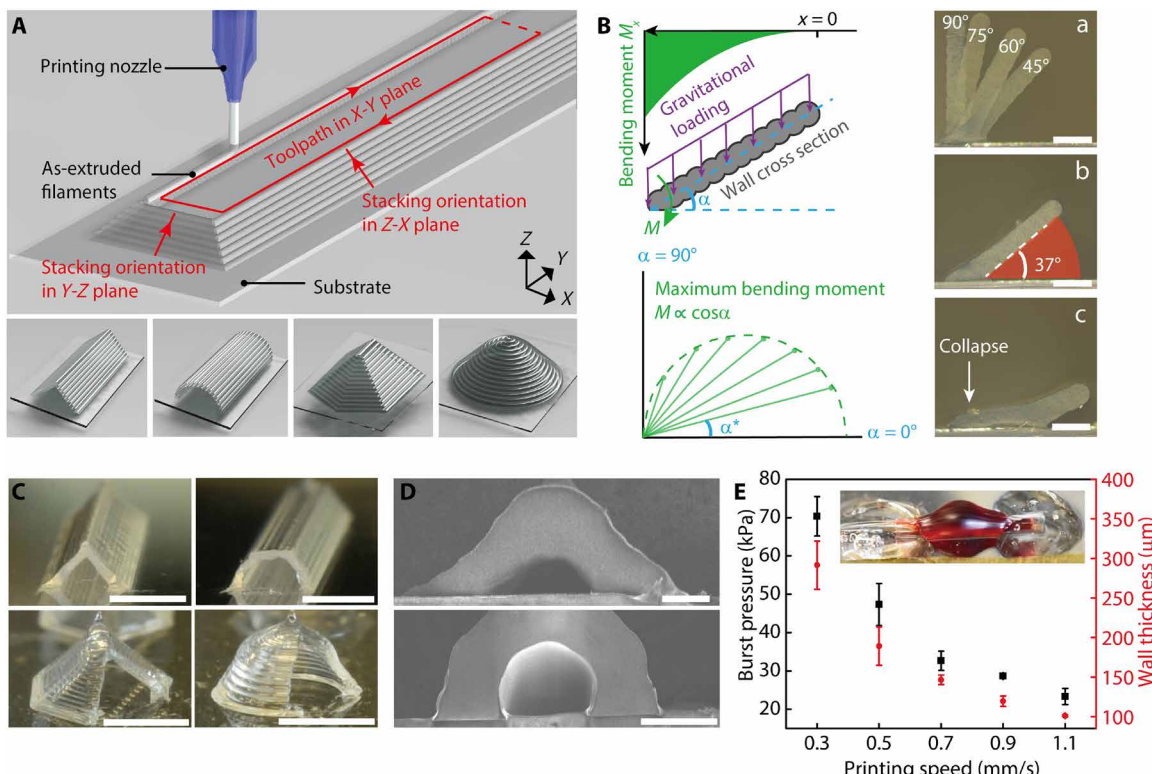


**Fig. 1. 3D printed self-supporting microfluidic structures.** (A) Top: Schematic of 3D printing a microfluidic channel. Bottom: 3D models of self-supporting structures including triangular channel, circular channel, hexagonal dome, and conical dome. (B) Left: Bending moment analysis of a self-supporting wall printed with the straight profile. Right: (a) Composite cross-sectional images of silicone walls of varying incline angles and an overhang length of 700  $\mu\text{m}$ . The boundary of each individual image is distinguished by the edge of the wall. (b) 37° was found to be the smallest incline angle that can be printed. (c) A silicone wall printed at an incline angle below 37° collapsed at the root. Scale bars, 200  $\mu\text{m}$ . Photo credit: Ruitao Su, University of Minnesota. (D) SEM images of triangular and circular channels with a width of ca. 100  $\mu\text{m}$ . Scale bars, 100  $\mu\text{m}$ . Photo credit: Ruitao Su, University of Minnesota. (E) Plot of burst pressure and wall thickness of the triangular channels with respect to printing speed ( $N = 3$ ). The inset photo shows one specimen under test with a length of 5 mm and a wall thickness of ca. 150  $\mu\text{m}$ . Photo credit: Ruitao Su, University of Minnesota.

We used a cantilever beam model with evenly distributed gravitational loading to analyze the distribution of the bending moment along the silicone walls (Fig. 1B)

$$M_x = \frac{\gamma}{2\cos(\alpha)} x^2 \quad (1)$$

$$M = \frac{1}{2} \gamma l^2 \cos(\alpha) \quad (2)$$

where  $M_x$  is the bending moment of a cross section at location  $x$ ,  $\gamma$  is the linear specific weight of the silicone wall,  $\alpha$  is the wall incline angle,  $M$  is the maximum bending moment at the root of the wall, and  $l$  is the total length of the wall. This model shows that the magnitude of the bending moment increases parabolically in the direction toward the substrate, making the root of the wall the weakest point. For a fixed length of the wall, the maximum bending moment increases as the incline angle decreases. An analogous analysis of the silicone wall with circular profiles is included in the Supplementary Materials (fig. S2).

Our printing results showed that, for the as-printed silicone walls in the submillimeter regime, the yield strength of the as-printed silicone ink is sufficient to balance the bending moment induced by gravity within a certain angular range. No sagging or collapse of the uncured structures was observed (Fig. 1B, a and b) before reaching a critical angle,  $\alpha^*$ . The smallest angle tested for the RTV silicone wall was  $37^\circ$  with a wall length of  $700 \mu\text{m}$ , below which the self-supporting wall collapsed (Fig. 1B, c). A stress state analysis based on the maximum shear stress criterion showed that the measured critical angle falls in the expected range of yield angles (fig. S3, A to C). Uncured RTV silicone exhibits the mechanical behavior of a yield-stress fluid, with storage modulus greater than loss modulus at low frequency (fig. S3D) (24). This renders a yield stress that must be overcome to initiate flow under the gravitational loading. Because the RTV silicone starts curing instantaneously after dispensing, as evidenced by the increasing storage modulus over time, the predicted yield strength is slightly higher than the measured value. RTV silicone also exhibits shear thinning behavior in the uncured state. Briefly, it displays an apparent viscosity of ca.  $10^4 \text{ Pa}\cdot\text{s}$  at a shear rate of  $0.01 \text{ s}^{-1}$ , and the viscosity decreases to ca.  $10^{-3} \text{ Pa}\cdot\text{s}$  as the shear rate increases to  $1000 \text{ s}^{-1}$  (fig. S3E). This variation in viscosity leads to a relatively low dispensing pressure, ca. 175 psi with  $100\text{-}\mu\text{m}$  nozzles, and a stronger resistance to creep for the as-printed structures.

With the mechanical equilibrium states above the critical angle, the silicone walls could then be printed into enclosed channels and chambers with designed geometries based on the toolpaths in the X-Y plane and the vertical stacking angle (Fig. 1C and movie S1). Channels with triangular and circular cross-sectional profiles and chambers with hexagonal and conical profiles were demonstrated. The channel dimension was controlled by specifying the distance between the sidewalls and the incline angle. The thicknesses of the extruded filaments, calibrated with the nozzle size and extrusion pressure, were offset in the design of the printing toolpath (fig. S4). Scanning electron microscopy (SEM) images show 3D printed microfluidic channels with an inner width down to  $100 \mu\text{m}$  (Fig. 1D).

The self-supporting microfluidic structures printed with RTV silicone have a distinct form factor compared to conventional microfluidic devices, for which a slab of PDMS or photocured resins are typically used to encase the microfluidic passages. The structures demonstrated here were simply composed of the substrates and fluid-

guiding channels, minimizing the total material volume of the final devices. One potential trade-off is a compromised burst pressure, i.e., the channels failing under a relatively low internal pressure. We investigated the burst pressure of channels that were printed with varying wall thicknesses by changing the printing speed. Keeping the dispensing pressure and nozzle size constant, slower printing speed generated thicker sidewalls since more ink was extruded for a given length of channel. With a moderate wall thickness of ca.  $200 \mu\text{m}$ , the printed microfluidic channels demonstrated an average burst pressure above  $40 \text{ kPa}$  (Fig. 1E and movie S2). For comparison, the backpressure applied to actuate aqueous flows in most microfluidic applications rarely exceeds  $10 \text{ kPa}$  (25, 26). Computational fluid dynamic (CFD) simulations showed that the devices demonstrated in this work required back pressures below  $1 \text{ kPa}$ , and the devices were repeatedly tested with no observable leakage.

Next, by precisely designing printing toolpaths, multifunctional microfluidic constituents including channel-chamber transitions, T-shaped intersections, and overlapping channels could be printed with the self-supporting structures. Our methodology of printing microfluidic devices consists of the following steps: (1) mathematically reconstruct the target surface geometry and design the routing and geometry of microfluidic channels to incorporate predeposited elements; (2) generate continuous and conformal printing toolpaths considering channel width, filament diameter (fig. S4), wall incline angle, and overlapping of adjacent filaments; (3) execute the printing in the order of (i) microstructures within the channels, (ii) microfluidic channels and chambers, and (iii) encapsulation materials for valves and pumps; and (4) after the microfluidic structures are fully cured for ca. 5 hours under ambient conditions, cut openings on the predefined channel terminals and insert connection tubes, applying sealants to create airtight connections. The high elasticity of cured silicone channels enabled a facile and tight connection to external tubing.

### 3D printed microfluidic mixers

Microfluidic mixers are important components for the rapid mixing of chemical species in the typical low Reynolds number flow of microfluidic applications (27). Monolithic mixers have been fabricated by soft lithography (28, 29) and additive manufacturing (30, 31). Extrusion-based printing allows for the convenient incorporation of multiple materials within the same structure (32). To demonstrate the high geometric modeling accuracy of this methodology, we 3D printed microfluidic mixers with self-supporting silicone channels and embedded polycaprolactone (PCL) HB ridges. The mixers consisted of a T-shaped inlet intersection and a main mixing channel where the HB ridges were housed. Five sets of HB ridges with variable heights were embedded within the  $990\text{-}\mu\text{m}$ -wide mixing channels (fig. S5). Three steps were adopted to print the mixers (Fig. 2A). First, we printed the HB ridges on the polyethylene terephthalate (PET) substrates with an interlayer resolution of  $30 \mu\text{m}$ . PCL dissolved in dichloromethane was used as the ink, and rigid HB ridges were formed following rapid evaporation of the solvent. Then, to print the base, i.e., the lower channels including the T-shaped intersections, continuous and cycling printing toolpaths were executed to eliminate the disruption to the ink dispensing. Last, after the lower channels were closed, the nozzle was lifted and translated to the next higher channel that remained open, and another continuous toolpath was executed to close the roof. The specifically designed continuous toolpaths prevented discrepancies in filament connection, creating leakage-free channel intersections and transitions between

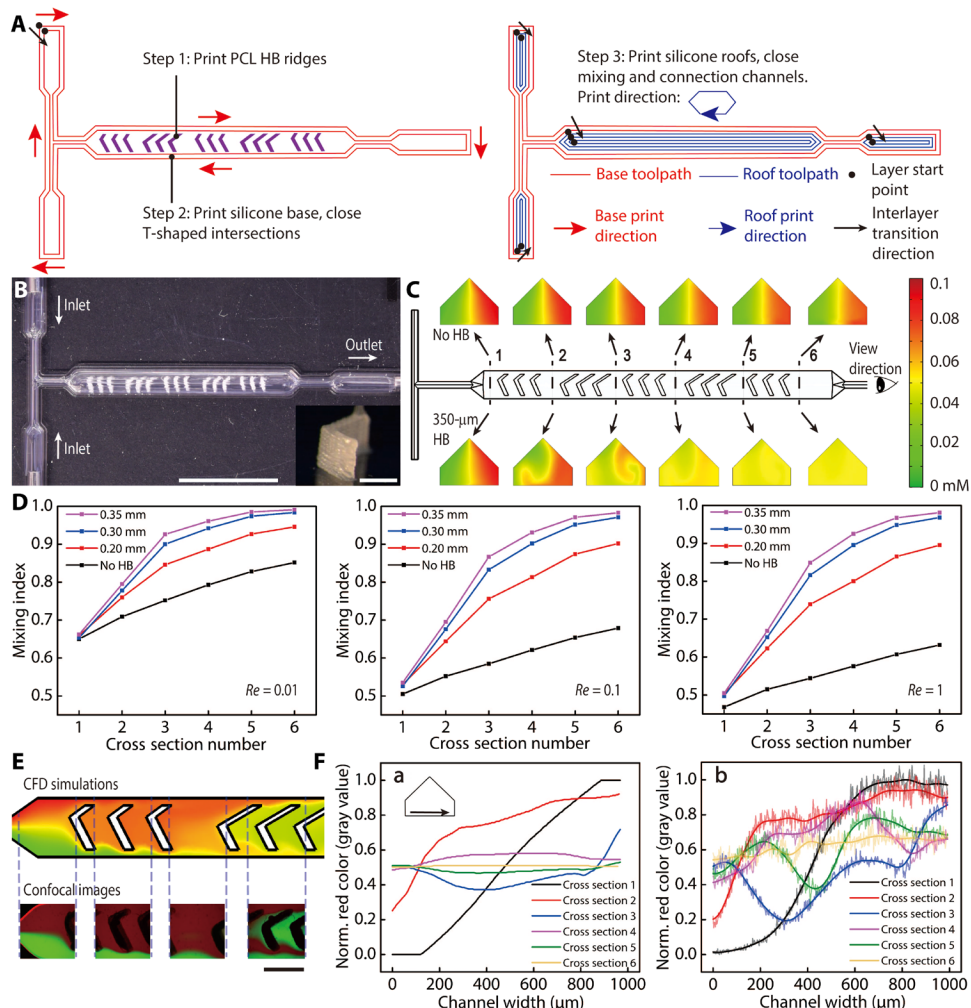


**Fig. 2. 3D printed multimaterial microfluidic mixers.** (A) Three-step printing procedure of the mixers. Continuous toolpaths were designed to minimize disruption in ink extrusion and realize leakage-free connections between channels. (B) Top view of the 3D printed mixer. Scale bar, 5 mm. The inset photo shows one HB ridge printed with PCL. Scale bar, 300  $\mu\text{m}$ . Photo credit: Ruitao Su, University of Minnesota. (C) CFD simulation of chemical species mixing at six cross sections with  $Re = 1$ . The mixing evolutions along the mixing channel without and with HB ridges (350  $\mu\text{m}$ ) are displayed in the top and bottom panels, respectively. (D) Plots of the simulated mixing indices with different heights of HB ridges within the Stokes flow regime ( $Re \leq 1$ ). (E) Comparison between the color maps of simulated concentration and confocal images at selected sections along the mixing channels. The imaging plane is 10  $\mu\text{m}$  above the substrate.  $Re = 1$ . HB height is 350  $\mu\text{m}$ . Scale bar, 500  $\mu\text{m}$ . Photo credit: Ruitao Su, University of Minnesota. (F) Comparison of red color intensity across the mixing channel at the above six cross sections between (a) simulated color maps and (b) confocal images. Data in plot (b) were transformed by a Fourier low-pass filter.

differently sized channels. Figure 2B demonstrates a 3D printed mixer that was embedded with 350- $\mu\text{m}$ -tall HB ridges.

Next, we validated the performance of the mixers with CFD simulation and confocal microscopic imaging. CFD models were built in the Stokes flow regime, where the Reynolds number is no greater than one ( $Re \leq 1$ ). The two inlets were each inputted with solutions of dextran (ca. 10 kDa) that were modified with rhodamine B (red) or fluorescein isothiocyanate (FITC) (green), respectively. The input solutions had an initial concentration of 0.1 mM. Figure 2C compares the mixing effects of two mixers at  $Re = 1$ , one without HB ridges (top row) and one with 350- $\mu\text{m}$ -tall embedded HB ridges (bottom row). An inspection of six selected cross sections along the channels showed improvement in the extent of mixing, with the latter generating a well-mixed output. We quantitatively evaluated the mixing effect with the mixing index  $W$

$$W = 1 - \frac{\sigma}{\sigma_{\max}} \quad (3)$$

where  $\sigma$  is the SD of the concentration of one selected species within a cross section and  $\sigma_{\max}$  is the SD at the entrance of the mixing channel. Therefore,  $W$  is in the range of [0,1] and increases with the extent of mixing.

As expected, the mixing indices increased along the channel as the solutions flowed through the mixing channels even in the cases of no embedded HB ridges, as partial mixing was induced by molecular diffusion (Fig. 2D). This was also validated by the decreasing intensities of red and green colors from cross sections 1 to 6 in the top row of Fig. 2C. Because a higher flow rate results in a shorter time for solutions to mix in the channels, the extent of mixing induced by diffusion decreases as  $Re$  increases. Our simulation showed that even at  $Re = 1$ , the mixing index at the outlet approached the maximum

with an HB ridge height of 350  $\mu\text{m}$ . The enhancement of mixing was attributed to the local turbulence induced by the embedded PCL HB ridges. To confirm that the CFD simulations represented the real mixing scenario, we acquired confocal microscopic images of the flow fields in the mixing channels. The experimental steady-state flow patterns displayed high fidelity to the computational model conducted with identical boundary conditions (Fig. 2E and fig. S6). Furthermore, the distribution of red color intensity was measured across the above six cross sections for both simulated color maps and confocal images (Fig. 2F). The shape and relative magnitude of the intensity curves demonstrated a good agreement, and a comparable mixing efficacy to SL printed mixers was observed within the 13-mm-long mixing channel (30).

### Microfluidic-integrated salinity sensor

There has been a persistent effort to integrate microfluidics with electronic sensors to create high-throughput sensing platforms (33, 34). These systems can suffer from either the time-consuming process involved with soft lithography (35), stamp distortions, misalignment issues and resulting surface contamination, or a bulky encapsulation for the microfluidic components (21, 36). The self-supporting microfluidic structures fabricated with extrusion-based 3D printing provides a previously undiscovered solution to seamlessly merge fluidics and electronics. To this end, we directly printed microfluidic structures on a microfabricated salinity sensor array, realizing synchronous alignment and integration during the printing process.

Gold electrodes and alignment marks were predeposited on a silicon wafer, and serially connected microfluidic channels and chambers were printed on top of the sensor array (Fig. 3A). Each salinity sensor consisted of a pair of gold electrodes that were housed inside the printed microfluidic chamber and used to measure the impedance of NaCl solutions flowing over the sensor. A simplified model of the measurement circuit included two double-layer capacitors and an equivalent parallel capacitor-resistor unit.

Before printing, the alignment marks were used to position the sensor array in the designed location within the coordinate system of the printer. Then, the printing was conducted by extruding the silicone ink to construct the self-supporting microfluidic structures (Fig. 3B). Continuous printing toolpaths similar to the microfluidic mixers were designed. The base was first printed to close the lower channels, and then, the roofs were printed to close the remaining chambers. A robust adhesion formed between the substrate and printed parts after the RTV silicone cured under ambient conditions, creating a compact form factor that guided the flow of analyte solutions on the sensors (Fig. 3C). Impedance measurements were then conducted with the hybrid microfabricated/3D printed salinity sensor. The microfluidic channels and chambers have a total internal volume of 20.87  $\mu\text{l}$ , and a flow rate of 50  $\mu\text{l}/\text{min}$  was used for the impedance measurement. CFD simulations showed highly laminar flow within the sensor (fig. S7A) and a back pressure of ca. 6 Pa (Fig. 3D) at the inlet, well below the burst pressure of the silicone structures. Therefore, the microfluidic-integrated sensor demonstrated

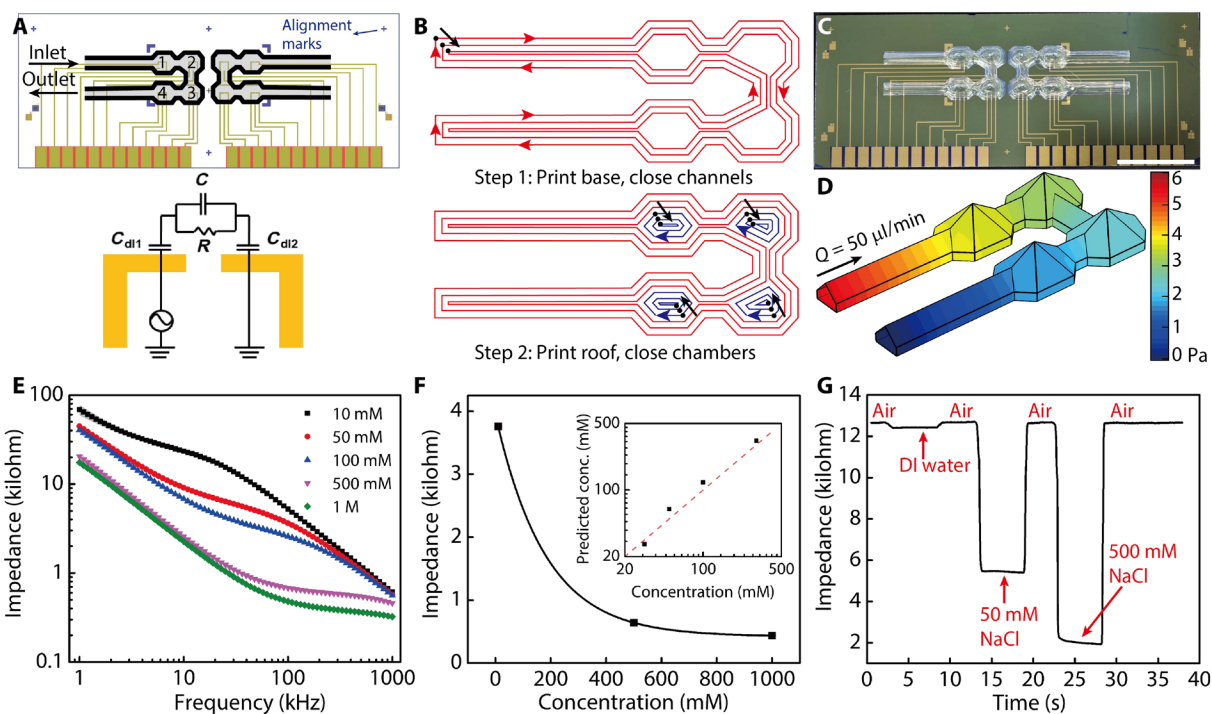


**Fig. 3. Microfluidic-integrated salinity sensor consisting of microfabricated sensor arrays and 3D printed channels and chambers.** (A) Layout of gold electrodes and alignment with microfluidic structures on the salinity sensor and a model of the measurement circuit.  $C_{dl}$ , double layer capacitance. (B) A two-step printing procedure was used to realize leakage-free connections between self-supporting channels and chambers. (C) Image of the microfluidic-integrated salinity sensor before connection to external tubes. Scale bar, 5 mm. Photo credit: Ruitao Su, University of Minnesota. (D) CFD simulated pressure distribution on the silicone wall under a flow rate of 50  $\mu\text{l}/\text{min}$ . (E) Plot of impedance spectra of different NaCl solutions measured with sensor 1 from 1 to 1000 kHz ( $n = 5$ ). (F) Calibration curve of the salinity sensor that was fitted with an exponential decay function. The inset plot displays the concentration prediction of four NaCl solutions with the salinity sensor. The impedance was measured at 145 kHz. (G) Real-time impedance measurement at 60 kHz of deionized (DI) water and 50 and 500 mM NaCl solutions that were flowed through the salinity sensor. The baseline denotes the impedance measured with an empty sensor.

good structural integrity, and no leakage was observed during our tests.

AC signals were applied to the electrodes, and frequency sweeps were conducted in the range of 1 to 1000 kHz as NaCl solutions of different concentrations were flushed over the sensor. The acquired impedance spectra were in good agreement with the literature (37), and high repeatability was observed for the four sensors in the tested array (Fig. 3E and fig. S7, B to D). To use the device as a salinity sensor, we calibrated sensor 1 with the measured impedance of NaCl solutions and found that the impedance-concentration relationship of NaCl solutions at 145 kHz could be fitted closely with the exponential decay equation

$$Z = A e^{(-c/t)} + Z_0 \quad (4)$$

where  $Z$  is the impedance of the NaCl solutions measured at 145 kHz;  $c$  is the molar concentration of the solutions; and  $A$ ,  $t$ , and  $Z_0$  are the fitted parameters (Fig. 3F). With this model, accurate predictions of NaCl concentrations were obtained by the 3D printed salinity sensor. Real-time and dynamic salinity sensing is important for applications such as seawater purification and ocean environment monitoring (38). To demonstrate the real-time impedance measurement with the salinity sensor, deionized (DI) water and 50 and 500 mM NaCl solutions were sequentially flushed over the sensor with air gaps in between while the frequency was held at 60 kHz. Using the impedance measured at the air-filled state as the baseline, the impedance change induced by salt concentrations was clearly observed (Fig. 3G and movie S3). The combination of microfabrication and 3D printing represents a compelling strategy for automatable production of biochemical sensors. We envision that this sensing platform could be extended to wider applications such as high-throughput biochemical diagnostic assays through the integration of sensing arrays that are functionalized with probing molecules including DNA and antibodies. Each sensor of the device can be functionalized via 3D printing to create diverse sensing arrays for the multiplexed detection of various targets within one microfluidic chip.

### Automation components and 3D microfluidics

Next, we demonstrate that the printing toolpaths can be designed to conformally accommodate the target surface, realizing microfluidic automation components and previously unrealized 3D microfluidics. Automation components including valves and pumps are critical to the control and actuation of microfluidic devices. Pneumatically actuated microfluidic valves and pumps were previously demonstrated by Unger *et al.* (39) using microfabrication and have recently been replicated via 3D printing toward the goal of high-throughput and low-cost manufacturing (11, 40). With the extrusion-based 3D printing method, the self-supporting microfluidic structures can be readily applied to create functional microfluidic valves and pumps that are conformal to curvilinear surfaces via overlapping silicone channels and encapsulation (Fig. 4A).

The 3D printed microfluidic valves consisted of one flow channel that permitted the liquid to traverse and one control channel that was conformally printed over the flow channel (movie S4). An enclosed hollow space was thereby created between the two channels to act as a valve when actuated by pressurized gas. The valve section, i.e., the crossing junction of the two channels, was then encapsulated and hardened by a UV-curable acrylate ester-based resin so that only downward expansion of the pressurized gas in the control

channel was allowed to close the valve (Fig. 4B). Here, the highly elastic silicone wall provided a flexible native membrane to open or close the valve. The control channel could be conveniently interfaced with external tubes and sealed directly with the encapsulation resin (fig. S8), which maintained its seal at an air pressure of up to 600 kPa. Generally, a higher flow pressure required a correspondingly higher closing pressure to stop the flow. For the closing pressure tests of the valve (fig. S9), a 300-kPa controlling pressure closed the valve completely, while a hydraulic pressure up to 30 kPa was applied to the flow channel (Fig. 4C and movie S5). Furthermore, peristaltic microfluidic pumps can also be directly 3D printed using three controlling channels laid out in parallel and encapsulated as one unit. The microfluidic pump was operated by activating the control channels according to a three-phase peristaltic code. Longer actuation times yielded a more complete shutoff of the control channels and therefore could be tuned to generate a higher pumping volume per cycle. On the basis of our tests, a flow rate of 105 nl/cycle was achieved with an actuation pressure of 100 kPa and an actuation time of 1.2 s (Fig. 4D).

Emerging microfluidics-based biomedical applications such as physiological status monitoring via sweat collection and sensing require the direct integration of microfluidic networks conformally onto curvilinear surfaces such as human skin (41). The high flexibility and stretchability of the 3D printed self-supporting structures provide a promising new avenue to next-generation wearable microfluidic devices (figs. S10 and S11). Spatially structured toolpaths allow us to transcend the conventional 2D microfluidic form factor and directly “write” self-supporting microfluidic structures onto 3D targets. As a demonstration, we designed and printed converging and serpentine microfluidic channels onto a spherical surface (the outer surface of a 10-ml glass flask) with simultaneously integrated valves (Fig. 4E and movie S6). To generate the toolpaths of the 3D microfluidic network, the channel routes and valve structures were first projected onto a planar surface (Fig. 4F). The local cross-sectional profiles of the channels were then inspected by extending the individual filaments onto the corresponding spherical layers. The filament stacking schemes were specifically designed to ensure an even spacing between adjacent filaments. As the microfluidic channel was placed further away from the sphere center, the cross-sectional profile became less symmetric, with the outer half being more extended. Therefore, extra “spacer” filaments were needed to prevent the collapse and clogging of the channels (Fig. 4F, a to c). The cross-sectional profiles of the spherical microfluidic channels closely resemble the designed filament stacking schemes. Controlled by the two integrated valves, the liquid sources could be selected, either as a single input or the mixing of two inputs, to enter the serpentine channel, and further guided to flow across the spherical surface (movie S7).

### DISCUSSION

This work presented an extrusion-based 3D printing methodology for the automatable fabrication of self-supporting elastomeric structures using a one-part acetoxy silicone. Mechanical equilibrium states of the as-printed silicone walls enabled the printing of hollow microfluidic channels and chambers without supporting materials in the submillimeter regime. Channel widths down to 100 μm were printed. While the burst pressure of the elastomeric channels was relatively low because of the single-wall structure, it is still at least one order of magnitude higher than the typical pressures required

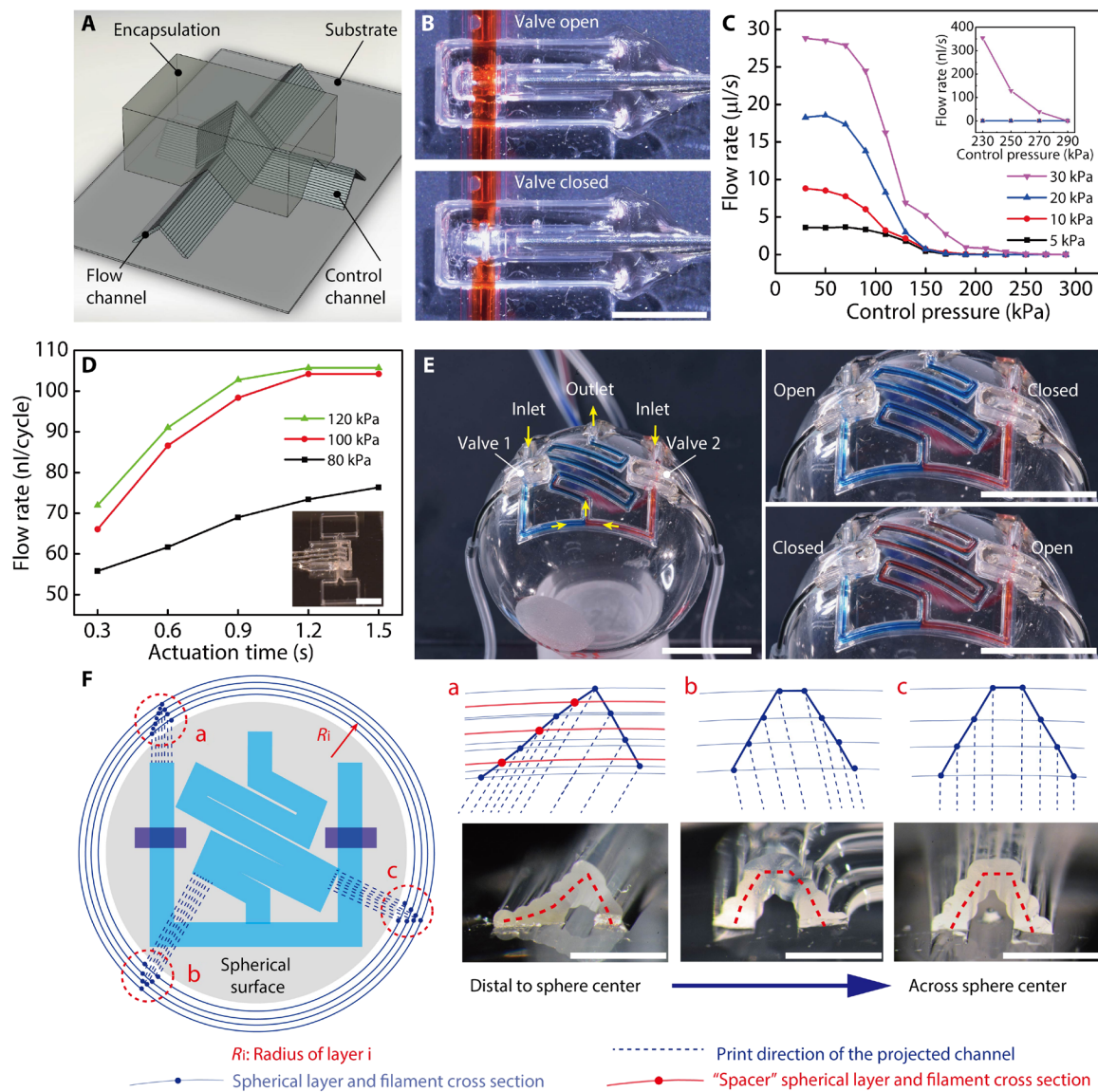


**Fig. 4. 3D printed microfluidic valve, pump, and spherical microfluidic network.** (A) Schematic displaying the configuration of the 3D printed microfluidic valve. (B) Photos displaying the open and closed states of the 3D printed microfluidic valve. The valve was closed with a pressure of 100 kPa. Scale bar, 3 mm. Photo credit: Ruitao Su, University of Minnesota. (C) Closing pressure test of 3D printed microfluidic valve under varying flow pressures. (D) Flow rate test of a microfluidic pump. The pump was actuated with a standard peristaltic code: 001, 100, and 010, where 1 and 0 denote the open and closed state, respectively. The inset image displays a 3D printed microfluidic pump with two liquid reservoirs. Scale bar, 5 mm. Photo credit: Ruitao Su, University of Minnesota. (E) 3D printed spherical converging and serpentine microfluidic channels with integrated valves. The images show three combinational operation states of valves 1 and 2. Scale bars, 10 mm. Photo credit: Ruitao Su, University of Minnesota. (F) Filament stacking schemes of the spherical microfluidic channels. (a) to (c) demonstrate the designed and printed profiles of three channel cross sections. Spacer filaments were added to prevent the collapse of asymmetric channels that were distal to the sphere center. Scale bars. 1 mm. Photo credit: Ruitao Su, University of Minnesota.

Downloaded from https://www.science.org on July 29, 2022

in most microfluidic applications to actuate aqueous flows. In addition, the 3D printed microfluidic channels that were encapsulated with UV-curable resins had sufficient mechanical strength to enable automation components including microfluidic valves and pumps.

By specifically designed continuous printing toolpaths, leakage-free microfluidic constituents including T-shaped intersections, connections between channels and chambers, and overlapping channels were realized, which facilitated concise integration with predeposited 3D structures and electronic sensors. By this means, multimaterial microfluidic mixers were created, and the mixing ef-

ficacy was validated using both CFD simulations and confocal microscopic imaging. A microfluidic-integrated sensor chip was fabricated by directly printing serially connected channels and chambers onto microfabricated salinity sensors, enabling a hybrid platform between top-down lithography-based microfabrication and bottom-up microfluidic patterning via 3D printing. Notably, a 3D microfluidic network integrated with valves was directly printed onto a spherical surface, and successful control over the flow in the converging and serpentine channels was demonstrated. With further generalization, we envision that this methodology could be extended

to freeform surfaces such as human skin for directly 3D printed physiological sensors (42).

In future work, the performance and functionality of the 3D printed microfluidic devices will be further enhanced and expanded. For instance, (i) higher channel resolution could be achieved by selecting smaller nozzles and tuning printing parameters; (ii) the burst pressure can be increased via multilayer printing to meet the pressure requirements of some applications; (iii) sensing arrays could be individually functionalized on the 3D printer and incorporated in the microfluidic sensors for multiplexed biochemical sensing; (iv) methodologies to control wall roughness could be studied for applications that involve issues such as rapid heat transfer and cell adhesion; and (v) large-scale integration, automation, and multi-functional fluid handling could be performed for automated diagnostic assays (43). Overall, extrusion-based 3D printing was demonstrated here as a versatile tool to fabricate both conventional and next-generation multifunctional microfluidic structures and devices.

## MATERIALS AND METHODS

### Materials

One-part acetoxy silicone (Loctite SI 595 CL) and two-part epoxy (Loctite EA E-00NS) were purchased from Henkel. PCL (440744), dextran–rhodamine B (dextran-RB; R8881), dextran–FITC (FD10S), and sodium chloride (NaCl; 31434) were purchased from Sigma-Aldrich. UV-curable resin, a blend of acrylate esters and amine-modified acrylate esters (PRO-001 UV), was purchased from NovaCentrix.

### Printing self-supporting microfluidic structures

First, the diameters of extruded silicone filaments were characterized with a microscope (Leica DM4500) and correlated to printing parameters including the inner diameter of the printing nozzles (Nordson EFD), dispensing pressure (Ultimus V Dispenser, Nordson EFD), and translational speed. Next, the stacking orientation and spacing between adjacent filaments was calculated to ensure a 30 to 50% overlap. After the microfluidic routes and geometry of the substrate were determined, 2D continuous toolpaths of the printing nozzle were designed with the software CADFusion (Aerotech Inc.). To generate the printing toolpaths for the spherical microfluidics, the cross sections of channels with different distances to the sphere center were inspected, and spacer layers were added to ensure even spacing between adjacent filaments. A MATLAB script was then used to divide the 2D toolpaths into 50-mm (20 mm for valves) straight elements, and the Z coordinates were calculated on the basis of the radii of the corresponding layers. The calculated coordinates were written into G-code and outputted from the MATLAB script.

To clean the target surfaces, PET films and spherical glass flasks were sonicated in acetone, isopropanol, and DI water sequentially for 5 min each and blown-dry with high-purity nitrogen (99.998%). Then, the uncured silicone ink was extruded on a robotic gantry system (AGS1000, Aerotech Inc.) to print the microfluidic structures on the target surfaces. For the microfluidic mixers, the HB ridges in the mixing channels were printed with PCL that was dissolved in dichloromethane at a concentration of 20 weight %, which was then printed with a pressure of 35 psi and speed of 0.2 mm/s. The inter-layer resolution of HB ridges was 30  $\mu\text{m}$ , and the printing nozzles had an inner diameter of 80  $\mu\text{m}$  (TE734025PK, Techcon Inc.). The printed structures were fully vulcanized in air for 5 hours before testing. Metal tubes (23 to 25 gauge; Nordson EFD) were inserted

into the 3D printed silicone channels and sealed with epoxy to connect with external liquid sources.

### CFD simulation of the chemical species mixing

The CFD simulation was conducted with the finite element analysis (FEA) software COMSOL Multiphysics (COMSOL Inc.). Two modules, laminar flow and transport of diluted species, were coupled to simulate the chemical species mixing. The laminar flow was simulated on the basis of the continuity and Navier-Stokes equations

$$\nabla(\rho\mathbf{u}) = 0 \quad (5)$$

$$\rho\mathbf{u} \cdot \nabla\mathbf{u} = -\nabla p + \nabla(\mu(\nabla\mathbf{u} + (\nabla\mathbf{u})^T)) \quad (6)$$

where  $\mathbf{u}$  is the fluid velocity,  $p$  is the fluid pressure,  $\rho$  is the fluid density, and  $\mu$  is the fluid dynamic viscosity. The transport of diluted species was simulated on the basis of the convection-diffusion equation

$$\frac{\partial c_i}{\partial t} + \nabla(-D_i \nabla c_i + c_i \mathbf{u}) = 0 \quad (7)$$

where  $c_i$  and  $D_i$  are the concentration and diffusivity of species  $i$ , respectively.

Water at 25°C was defined as the carrier fluid with a density of 1000 kg/m<sup>3</sup> and a dynamic viscosity of  $8.9 \times 10^{-4}$  Pa·s. Boundary conditions include a rigid and nonslippery wall, uniform velocity at the two inlets for different Reynolds numbers, input concentration of 0.1 mM for the two species, and a zero outlet pressure. Diffusivity of the fluorescent-labeled dextran molecules was calculated on the basis of the Stokes-Einstein equation

$$D = \frac{k_B T}{6\pi\mu R_H} \quad (8)$$

where  $D$  is the diffusivity of the investigated molecules,  $k_B$  is Boltzmann constant,  $T$  is temperature, and  $R_H$  is the hydrodynamic radius of the molecules. With a molecular weight of ca. 10 kDa, the dextran molecules were estimated to have a hydrodynamic radius of 6 nm and a diffusivity of  $4.02 \times 10^{-11}$  m<sup>2</sup>/s (44). For the meshing of the simulated geometry, an iterative increase in the number of nodes showed that 61,400 nodes are sufficient for the simulation. To evaluate the mixing indices according to Eq. 3, the concentration information of species A was extracted from a cut plane with 6900 points selected from an orthogonal grid on the plane.

### Confocal microscopic imaging

Images of the flow fields in the microfluidic channels were acquired on a laser-scanning confocal microscope (Nikon A1Rsi, Nikon Instruments Inc.). The wavelengths of the lasers used to excite the red and green fluorescence were 561 and 488 nm, respectively. The two molecules, dextran-RB and dextran-FITC, were dissolved in DI water at a concentration of 0.1 mM and injected into the mixers with a two-channel syringe pump (Model Fusion 100CR, Chemex Inc.). Fluorescence images of red and green channels were taken after the flow reached a steady state with an exposure time of 2.1 s. The two color channels were combined with ImageJ (1.52r; National Institutes of Health, USA), with which the quantitative intensity of the red channel was also measured.

## Fabrication and characterization of microfluidic-integrated salinity sensor

The salinity sensors were fabricated on 500- $\mu\text{m}$ -thick wafers that have an oxide layer of 300 nm (University Wafer Inc.). Electrodes (10/190 nm Cr/Au, line width of 100  $\mu\text{m}$ , 60  $\mu\text{m}$  separation within one channel) and alignment marks were deposited via standard photolithography procedures in the cleanroom. Before printing microfluidic structures, the sensor chips were cleaned by submerging in acetone, methanol, and isopropanol for 3 hours each, rinsing with DI water, and blowing dry with high-purity N<sub>2</sub>. During printing, the alignment marks were used to align the sensor chips with the coordinate system of the printer. The completed salinity sensors were housed in a multielectrode chip platform (ED-ME-CELL, MicruX Technologies), which was connected to a mini USB box via an insulation-displacement contact cable, allowing each channel to be individually addressed. The impedance measurement of DI water and NaCl solutions was conducted on a semiconductor device analyzer (B1500A, Keysight Technologies Inc.) as the sensor was flushed at a flow rate of 50  $\mu\text{l}/\text{min}$  via a two-channel syringe pump (Model Fusion 100CR, Chemyx Inc.). Real-time measurement of solution impedance was conducted at a frequency of 60 kHz.

## Fabrication and characterization of microfluidic valves and pumps

The microfluidic valves and pumps were fabricated by sequentially printing flow channels, control channels, and an encapsulation container with silicone (fig. S8). After the silicone structures were fully vulcanized, metal tubes were inserted into the control channels and the UV-curable resin was deposited in the encapsulation container, which was cured under 400-nm UV light for 5 min (WF-501B CREE XR-C, UltraFire). The flow rate of the microfluidic valve was measured via the mass of flowed solutions with a balance (MS304S, Mettler Toledo Inc.). The pumping rate of the microfluidic pumps was measured by capturing videos and measuring the traveling distance of the fluid within the transparent tubes (fig. S9).

## SUPPLEMENTARY MATERIALS

Supplementary material for this article is available at <http://advances.sciencemag.org/cgi/content/full/6/41/eabc9846/DC1>

## REFERENCES AND NOTES

- P. N. Nge, C. I. Rogers, A. T. Woolley, Advances in microfluidic materials, functions, integration, and applications. *Chem. Rev.* **113**, 2550–2583 (2013).
- E. Samiei, M. Tabrizian, M. Hoorfar, A review of digital microfluidics as portable platforms for lab-on-a-chip applications. *Lab Chip* **16**, 2376–2396 (2016).
- C. D. Chin, V. Linder, S. K. Sia, Commercialization of microfluidic point-of-care diagnostic devices. *Lab Chip* **12**, 2118–2134 (2012).
- D. Huh, B. D. Matthews, A. Mammoto, M. M. Zavala, H. Y. Hsin, D. E. Ingber, Reconstituting organ-level lung functions on a chip. *Science* **328**, 1662–1668 (2010).
- J. Wu, M. Gu, Microfluidic sensing: State of the art fabrication and detection techniques. *J. Biomed. Opt.* **16**, 080901 (2011).
- P. Kim, K. W. Kwon, M. C. Park, S. H. Lee, S. M. Kim, K. Y. Suh, Soft lithography for microfluidics: A review. *Biochip J.* **2**, 1–11 (2008).
- D. I. Walsh III, D. S. Kong, S. K. Murthy, P. A. Carr, Enabling microfluidics: From clean rooms to makerspaces. *Trends Biotechnol.* **35**, 383–392 (2017).
- X. Li, Z. T. F. Yu, D. Geraldo, S. Weng, N. Alve, W. Dun, A. Kini, K. Patel, R. Shu, F. Zhang, G. Li, Q. Jin, J. Fu, Desktop aligner for fabrication of multilayer microfluidic devices. *Rev. Sci. Instrum.* **86**, 075008 (2015).
- N. Bhattacharjee, A. Urrios, S. Kang, A. Folch, The upcoming 3D-printing revolution in microfluidics. *Lab Chip* **16**, 1720–1742 (2016).
- A. Naderi, N. Bhattacharjee, A. Folch, Digital manufacturing for microfluidics. *Annu. Rev. Biomed. Eng.* **21**, 325–364 (2019).
- C. I. Rogers, K. Qaderi, A. T. Woolley, G. P. Nordin, 3D printed microfluidic devices with integrated valves. *Biomicrofluidics* **9**, 016501 (2015).
- R. D. Sochol, E. Sweet, C. C. Glick, S. Venkatesh, A. Avetisyan, K. F. Ekman, A. Raulinaitis, A. Tsai, A. Wienkers, K. Korner, K. Hanson, A. Long, B. J. Hightower, G. Slatton, D. C. Burnett, T. L. Massey, K. Iwai, L. P. Lee, K. S. Pister, L. Lin, 3D printed microfluidic circuitry via multijet-based additive manufacturing. *Lab Chip* **16**, 668–678 (2016).
- J. A. Lewis, Direct ink writing of 3D functional materials. *Adv. Funct. Mater.* **16**, 2193–2204 (2006).
- S. H. Park, R. Su, J. Jeong, S. Z. Guo, K. Qiu, D. Joung, F. Meng, M. C. McAlpine, 3D printed polymer photodetectors. *Adv. Mater.* **30**, 1803980 (2018).
- M. Singh, Y. Tong, K. Webster, E. Cesewski, A. P. Haring, S. Laheri, B. Carswell, T. J. O'Brien, C. H. Aardema, R. S. Senger, J. L. Robertson, B. N. Johnson, 3D printed conformal microfluidics for isolation and profiling of biomarkers from whole organs. *Lab Chip* **17**, 2561–2571 (2017).
- B. N. Johnson, K. Z. Lancaster, I. B. Hogue, F. Meng, Y. L. Kong, L. W. Enquist, M. C. McAlpine, 3D printed nervous system on a chip. *Lab Chip* **16**, 1393–1400 (2016).
- D. Joung, V. Truong, C. C. Neitzke, S.-Z. Guo, P. J. Walsh, J. R. Monat, F. Meng, S. H. Park, J. R. Dutton, A. M. Parr, M. C. McAlpine, 3D printed stem-cell derived neural progenitors generate spinal cord scaffolds. *Adv. Funct. Mater.* **28**, 1801850 (2018).
- J. L. Erkal, A. Selimovic, B. C. Gross, S. Y. Lockwood, E. L. Walton, S. McNamara, R. S. Martin, D. M. Spence, 3D printed microfluidic devices with integrated versatile and reusable electrodes. *Lab Chip* **14**, 2023–2032 (2014).
- D. Therriault, S. R. White, J. A. Lewis, Chaotic mixing in three-dimensional microvascular networks fabricated by direct-write assembly. *Nat. Mater.* **2**, 265–271 (2003).
- V. Saggiomo, A. H. Velders, Simple 3D printed scaffold-removal method for the fabrication of intricate microfluidic devices. *Adv. Sci.* **2**, 1500125 (2015).
- T. Ching, Y. Li, R. Karyappa, A. Ohno, Y.-C. Toh, M. Hashimoto, Fabrication of integrated microfluidic devices by direct ink writing (DIW) 3D printing. *Sens. Actuators B Chem.* **297**, 126609 (2019).
- A. Z. Nelson, K. S. Schweizer, B. M. Rauzan, R. G. Nuzzo, J. Vermant, R. H. Ewoldt, Designing and transforming yield-stress fluids. *Curr. Opin. Solid State Mater. Sci.* **23**, 100758 (2019).
- A. Rahimi, A. Mashak, Review on rubbers in medicine: Natural, silicone and polyurethane rubbers. *Plast. Rubber Compos.* **42**, 223–230 (2013).
- H. A. Barnes, The yield stress—A review or ‘ταντά πει’—Everything flows? *J. Non-Newtonian Fluid Mech.* **81**, 133–178 (1999).
- T. Rodrigues, F. J. Galindo-Rosales, L. Campo-Deano, Towards an optimal pressure tap design for fluid-flow characterisation at microscales. *Materials* **12**, 1086 (2019).
- P. Cheung, K. Toda-Peters, A. Q. Shen, In situ pressure measurement within deformable rectangular polydimethylsiloxane microfluidic devices. *Biomicrofluidics* **6**, 26501–2650112 (2012).
- M. S. Williams, K. J. Longmuir, P. Yager, A practical guide to the staggered herringbone mixer. *Lab Chip* **8**, 1121–1129 (2008).
- B. Hama, G. Mahajan, P. S. Fodor, M. Kaufman, C. R. Kothapalli, Evolution of mixing in a microfluidic reverse-staggered herringbone micromixer. *Microfluid. Nanofluid.* **22**, 54 (2018).
- M. Wang, Z. Wang, M. Zhang, W. Guo, N. Li, Y. Deng, Q. Shi, A microfluidic chip with double-sided herringbone microstructures for enhanced capture of rare tumor cells. *J. Mater. Chem. B* **5**, 9114–9120 (2017).
- A. Enders, I. G. Siller, K. Urmann, M. R. Hoffmann, J. Bahnemann, 3D printed microfluidic mixers—A comparative study on mixing unit performances. *Small* **15**, 1804326 (2019).
- G. Comina, A. Suska, D. Filippini, Low cost lab-on-a-chip prototyping with a consumer grade 3D printer. *Lab Chip* **14**, 2978–2982 (2014).
- R. Su, S. H. Park, Z. Li, M. C. McAlpine, in *Robotic Systems and Autonomous Platforms*, S. M. Walsh, M. S. Strano, Eds. (Woodhead Publishing, 2019), pp. 309–334.
- D. Moschou, A. Tserepi, The lab-on-PCB approach: Tackling the μTAS commercial upscaling bottleneck. *Lab Chip* **17**, 1388–1405 (2017).
- M. C. McAlpine, H. D. Agnew, R. D. Rohde, M. Blanco, H. Ahmad, A. D. Stuparu, W. A. Goddard III, J. R. Heath, Peptide–nanowire hybrid materials for selective sensing of small molecules. *J. Am. Chem. Soc.* **130**, 9583–9589 (2008).
- M. Kim, W. Choi, H. Lim, S. Yang, Integrated microfluidic-based sensor module for real-time measurement of temperature, conductivity, and salinity to monitor reverse osmosis. *Desalination* **317**, 166–174 (2013).
- C. K. Tang, A. Vaze, J. F. Rusling, Automated 3D-printed unibody immunoarray for chemiluminescence detection of cancer biomarker proteins. *Lab Chip* **17**, 484–489 (2017).
- C. S. Widodo, H. Sela, D. R. Santosa, in *The 8th Annual Basic Science International Conference* (AIP Publishing, 2018), vol. 2021, p. 050003.
- M. Grossi, C. Parolin, B. Vitali, B. Ricci, Electrical impedance spectroscopy (EIS) characterization of saline solutions with a low-cost portable measurement system. *Eng. Sci. Technol. Int. J.* **22**, 102–108 (2019).
- M. A. Unger, H.-P. Chou, T. Thorsen, A. Scherer, S. R. Quake, Monolithic microfabricated valves and pumps by multilayer soft lithography. *Science* **288**, 113–116 (2000).

40. A. K. Au, N. Bhattacharjee, L. F. Horowitz, T. C. Chang, A. Folch, 3D-printed microfluidic automation. *Lab Chip* **15**, 1934–1941 (2015).
41. J. T. Reeder, J. Choi, Y. Xue, P. Gutruf, J. Hanson, M. Liu, T. Ray, A. J. Bandodkar, R. Avila, W. Xia, S. Krishnan, S. Xu, K. Barnes, M. Pahnke, R. Ghaffari, Y. Huang, J. A. Rogers, Waterproof, electronics-enabled, epidermal microfluidic devices for sweat collection, biomarker analysis, and thermography in aquatic settings. *Sci. Adv.* **5**, eaau6356 (2019).
42. Z. Zhu, S.-Z. Guo, T. Hirdler, C. Eide, X. Fan, J. Tolar, M. C. McAlpine, 3D printed functional and biological materials on moving freeform surfaces. *Adv. Mater.* **30**, 1707495 (2018).
43. J. Melin, S. R. Quake, Microfluidic large-scale integration: The evolution of design rules for biological automation. *Annu. Rev. Biophys. Biomol. Struct.* **36**, 213–231 (2007).
44. R. Peters, Nucleo-cytoplasmic flux and intracellular mobility in single hepatocytes measured by fluorescence microphotolysis. *EMBO J.* **3**, 1831–1836 (1984).

**Acknowledgments:** We thank X. Ouyang for assisting in taking images during the bending and stretching tests. We thank Z. Zhu for assisting in the setup of microfluidic pump tests. We thank Z. Fuenning and S. H. Park for suggestions and feedback on the manuscript preparation.

**Funding:** Research reported in this publication was sponsored by the Army Research Office, accomplished under Cooperative Agreement Number W911NF1820175 and basic research funding from the U.S. Army Combat Capabilities Development Command Soldier Center. The views and conclusions contained in this document are those of the authors and should not be interpreted as representing the official policies, either expressed or implied, of the Army Research Office or the U.S. government. The U.S. government is authorized to reproduce and distribute reprints for government purposes notwithstanding any copyright notation herein. This work was also supported by the National Institute of Biomedical Imaging and Bioengineering of the NIH under Award Number DP2EB020537. The content is solely the responsibility of the authors and does not necessarily represent the official views of the NIH. Further support came from the MnDRIVE program at the University of Minnesota. Confocal microscope imaging and analysis were performed at the University Imaging Centers

at the University of Minnesota. Portions of this work were conducted in the Minnesota Nano Center, which is supported by the NSF through the National Nano Coordinated Infrastructure Network (award number ECCS-1542202). **Author contributions:** R.S., M.S.W., J.R.U., and M.C.M. designed the study. R.S. printed and characterized the microfluidic structures and conducted the FEA simulations and confocal microscopic imaging. J.W., Q.S., and S.J.K. designed the templates and conducted the fabrication of the salinity sensor arrays. M.S.W. and R.S. measured the impedance of varying solutions with the microfluidic salinity sensors. R.S. wrote the first draft of the manuscript, and input and revisions were contributed by all authors. **Competing interests:** M.C.M. is in the Editorial Board of *Science Advances*. M.C.M., R.S., S.J.K., and J.R.U. are inventors on a provisional patent application entitled “Additively manufactured self-supporting microfluidics” related to this work filed on 10 September 2020, with the serial number 63/076,673. Two of the authors, S.J.K. and M.C.M., have signed preliminary understanding agreements regarding their appointment as members of the Scientific Advisory Board of GRIP Molecular Technologies Inc. The authors declare that they have no other competing interests. **Data and materials availability:** All data needed to evaluate the conclusions in the paper are present in the paper and/or the Supplementary Materials. Additional supporting data are available at the Data Repository for the University of Minnesota (<https://doi.org/10.13020/n1rk-nm34>) and from the authors upon request.

Submitted 25 May 2020

Accepted 26 August 2020

Published 9 October 2020

10.1126/sciadv.abc9846

**Citation:** R. Su, J. Wen, Q. Su, M. S. Wiederoder, S. J. Koester, J. R. Uzarski, M. C. McAlpine, 3D printed self-supporting elastomeric structures for multifunctional microfluidics. *Sci. Adv.* **6**, eabc9846 (2020).

## 3D printed self-supporting elastomeric structures for multifunctional microfluidics

Ruitao SuJiaxuan WenQun SuMichael S. WiederoderSteven J. KoesterJoshua R. UzarskiMichael C. McAlpine

*Sci. Adv.*, 6 (41), eabc9846. • DOI: 10.1126/sciadv.abc9846

**View the article online**

<https://www.science.org/doi/10.1126/sciadv.abc9846>

**Permissions**

<https://www.science.org/help/reprints-and-permissions>